Surface Green's functions and quasiparticle interference in Weyl semimetals

Sarah Pinon [1], Vardan Kaladzhyan,[2,*] and Cristina Bena[1]

[1]*Institut de Physique Théorique, Université Paris Saclay, CEA CNRS, Orme des Merisiers, F-91190 Gif-sur-Yvette Cedex, France*
[2]*Department of Physics, KTH Royal Institute of Technology, SE-106 91 Stockholm, Sweden*

We use the exact analytical technique introduced by us [Phys. Rev. B **101**, 115405 (2020)] to recover the surface Green's functions and the corresponding Fermi-arc surface states for various lattice models of Weyl semimetals. For these models we use the T-matrix formalism to calculate the quasiparticle interference patterns generated in the presence of impurity scattering. In particular, we consider the models introduced by Kourtis *et al.* [Phys. Rev. B **93**, 041109(R) (2016)] (model A) and Lau *et al.* [Phys. Rev. Lett. **119**, 076801 (2017)] (model B), and we find that, as opposed to observations previously obtained via joint density of states and spin-dependent scattering probability, the interarc scattering in the quasiparticle interference features is fully suppressed in model A, and is very small in model B. Our findings indicate that these models may not correctly describe materials such as $MoTe_2$, since for such materials interarc scattering is clearly visible experimentally, e.g., by Deng *et al.* [Nat. Phys. **12**, 1105 (2016)]. We also focus on the minimal models proposed by McCormick *et al.* [Phys. Rev. B **95**, 075133 (2017)], which indeed recover significant interarc scattering features.

I. INTRODUCTION

Recently, Weyl semimetals [1] have come into focus partly due to their exotic properties of exhibiting Weyl nodes, i.e., points at which the energy dispersion goes to zero and quasiparticles have a linear dispersion, as well as peculiar topological surface states, deemed Fermi-arc states. Typically these states appear at values of in-plane momentum lying on a line connecting the Weyl nodes, but for some of them the picture is modified by the appearance of surface electron/hole pockets; for these type of systems other nontopological surface states also arise. Such states, denoted track states, appear in momentum space as closed contours (as opposed to the Fermi-arc states).

A large amount of work, both theoretical [2–10] and experimental [11–23], has been devoted to the impurity scattering and the corresponding quasiparticle interference (QPI) features, and the possibility to extract information about the Weyl nodes, and hence Fermi arcs, from such features. However, the analysis of the QPI features is very complex, especially in the presence of both topological and trivial states simultaneously. The traditional methods to obtain the QPI features stem in general from first-principles calculations yielding information about the position, shape, and extension of Fermi arcs and track states in momentum space. Often a simple intuitive picture is constructed which assumes that the QPI features stem directly from a joint density of states (JDOS) of the underlying Fermi-arc states: In this picture each surface state is assumed to scatter by all the other existing surface states, and the resulting scattering momenta are counted to yield the QPI feature. The first correction to this picture takes into account the spin of each state and introduces a weight to the scattering processes based on the spins of each scattering pair of states.

However, these techniques are very crude and often fail to capture correctly the scattering processes and to predict the QPI features accurately. Their advantage, nevertheless, is that only basic information about the Fermi-arc states is required.

In order to calculate accurately the QPI features a more complex technique—the T-matrix formalism [24–27]—should be employed. The latter allows us to calculate exactly the Green's function (GF) of the system in the presence of a single impurity, and thus enables us to obtain the local density of states, as well as its Fourier transform, in the presence of impurity scattering. However, in order to apply the T-matrix formalism, information about the underlying surface Green's function of the system is required. The surface Green's functions of a given system cannot be computed very easily—in general, it requires iterative numerical techniques, hard to implement in a non-numerical community.

In a recent work [28] we proposed a simple and exact analytical technique that allows us to obtain the surface Green's functions of a three-dimensional system, with the only necessary ingredient being the bulk tight-binding Hamiltonian of the system. To summarize, the idea is to start with an infinite homogeneous three-dimensional system and then introduce the boundary as a two-dimensional planar scalar impurity with an impurity potential much larger than all the other energy scales of the problem [29]. This impurity effectively cuts the system in half and generates two two-dimensional infinite surfaces on the planes just below and above the impurity plane. The surface Green's functions for these surfaces are obtained using the T-matrix formalism, which for such a configuration provides an exact analytical solution for the full Green's functions of the infinite perturbed system, and thus also for the Green's function evaluated at positions adjacent to the impurity plane.

In this paper we use the technique from Ref. [28] to calculate the surface Green's functions for a number of models

*vardan.kaladzhyan@phystech.edu

proposed to describe Weyl semimetals: (1) the Kourtis [6] and Lau [8] models, minimal models that describe mostly type I Weyl semimetals with four Weyl points and two Fermi arcs, and (2) the McCormick model [7] based on a minimal helium model to describe both type I and type II four-Weyl-point systems with both Fermi arcs and topologically trivial track states. We subsequently use the resulting surface Green's functions and the T-matrix formalism to calculate the QPI features for these systems in the presence of a localized impurity at the surface. We find that in the Kourtis and Lau models the interarc scattering is almost entirely absent as a result of the spin structure of the Fermi-arc states. This is different from the results based on spin-dependent scattering probability (SSP) calculations in which the spin structure of the Fermi arcs reduces, but does not completely remove, the interarc features. As for the McCormick model, we identify features resulting from intra- and inter-Fermi-arc scattering, intra- and inter-track-state scattering, as well as scattering between the Fermi arc states and the track states.

The paper is organized as follows: In Sec. II we present the Kourtis and Lau models, their surface GFs, and the corresponding QPI patterns. In Sec. III we perform similar calculations for a model McCormick model, and we conclude in Sec. IV.

II. SURFACE GREEN'S FUNCTIONS AND QPI PATTERNS IN THE KOURTIS AND LAU MINIMAL MODELS FOR MoTe₂

We first consider the minimal models introduced in Refs. [6,8] to describe systems in the family of MoTe₂, i.e., Weyl semimetals with four Weyl points and two Fermi arcs per surface. The surface Green's functions and Fermi arcs, as well as their spin polarization have been obtained by the analytical technique presented in Ref. [28], thus below we summarize these findings, and proceed directly to computing the corresponding QPI features.

The tight-binding models described in Refs. [6,8], which we denote by $\mathcal{H}_1$ and $\mathcal{H}_2$, respectively, are described by the Bloch Hamiltonians given by

$$H_{1,2} = \sum_{\boldsymbol{k}} \psi^\dagger(\boldsymbol{k}) \mathcal{H}_{1,2}(\boldsymbol{k}) \psi(\boldsymbol{k}), \quad (1)$$

where $\psi(\boldsymbol{k}) = (c_{kA\uparrow}, c_{kA\downarrow}, c_{kB\uparrow}, c_{kB\downarrow})$ is a spinor with the index A/B denoting a generic unspecified orbital component, and $\uparrow / \downarrow$ the physical spin.

For the model in Ref. [6] written in the aforementioned basis we have

$$\mathcal{H}_1(\boldsymbol{k}) = g_1(\boldsymbol{k})\tau_1\sigma_3 + g_2(\boldsymbol{k})\tau_2\sigma_0 + g_3(\boldsymbol{k})\tau_3\sigma_0$$
$$+ g_0(\boldsymbol{k})\tau_0\sigma_0 + \beta\tau_2\sigma_2 + \alpha\sin k_y\tau_1\sigma_2, \quad (2)$$

where

$$g_0(\boldsymbol{k}) = 2d(2 - \cos k_x - \cos k_y),$$
$$g_1(\boldsymbol{k}) = a\sin k_x, \quad g_2(\boldsymbol{k}) = a\sin k_y,$$
$$g_3(\boldsymbol{k}) = m + t\cos k_z + 2b(2 - \cos k_x - \cos k_y), \quad (3)$$

and α, β are real parameters. The 2×2 identity matrices σ_0/τ_0 and the Pauli matrices σ_i/τ_i, $i = 1, 2, 3$, act in the spin
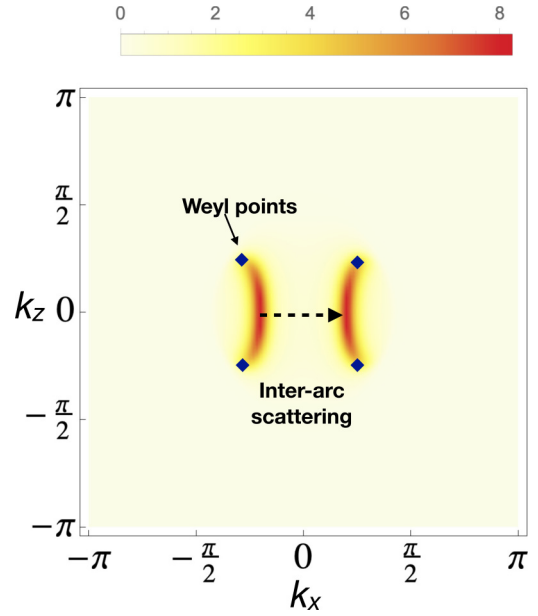

FIG. 1. The surface spectral function at $E = 0$ for the $\mathcal{H}_1$ model with parameters $a = b = 1$, $t = -1.5$, $d = m = 0$, $\beta = 0.9$. We clearly see the formation of two Fermi arcs.

and the orbital spaces, respectively, and side-by-side appearances of σ and τ matrices indicate tensor products.

We choose the following values of the parameters $a = b = 1$, $t = -1.5$, $d = m = 0$, $\beta = 0.9$, and $\alpha = 0.3$, corresponding to four Weyl points, and two Fermi arcs. The spectral function for the surface states $A(E, k_x, k_z) = -\frac{1}{\pi} \text{Im}\{\text{tr}[G_s(E, k_x, k_z)]\}$, as obtained in Ref. [28], is shown in Fig. 1. We should note that Fermi arcs appearing at the same surface have opposite spins, as derived in Ref. [28].

In what follows we start with the surface Green's functions for this model and we compute the surface QPI patterns in the presence of a surface impurity. We use the full T-matrix formalism yielding an exact solution to the problem provided the impurity is localized [i.e., delta function potential $V\delta(\boldsymbol{r})$, where $\boldsymbol{r}$ is in real space]. In this simple case the T-matrix is given by [24–27,30,31]

$$T(E) = \left[\mathbb{I} - V \int \frac{d\boldsymbol{k}}{(2\pi)^2} G_s(E, \boldsymbol{k}) \right]^{-1} V, \quad (4)$$

where $\mathbb{I}$ denotes the 4×4 identity matrix. Hereinafter we will set $V = \mathbb{I}$, which represents a scalar impurity covering a single site. Furthermore, we studied the effects of impurity strength variation by setting $V = U\mathbb{I}$, with $U \neq 1$. We have also studied the effects of magnetic impurities, and double-impurity scattering on the QPI patterns. However, we observed that these effects do not alter the main conclusion of our paper, and thus we leave these findings to Appendix B.

Generally, in most experiments QPI patterns corresponding to the Fourier transform of the local density of states at a given energy are measured, namely, $\delta\rho(\boldsymbol{k}, E) = \int d^2\boldsymbol{r}\, \delta\rho(\boldsymbol{r}, E) e^{-ik\boldsymbol{r}}$. In the T-matrix formalism this is given by

$$\delta\rho(\boldsymbol{k}, E) = \frac{i}{2\pi} \int \frac{d\boldsymbol{q}}{(2\pi)^2} \text{tr}[g(E, \boldsymbol{q}, \boldsymbol{k})], \quad (5)$$
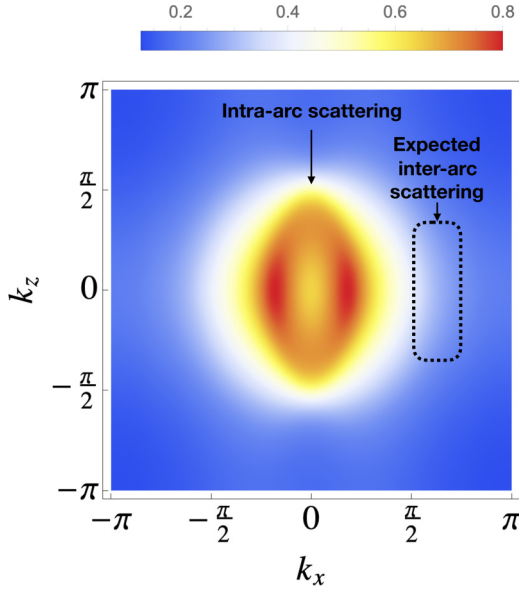
FIG. 2. QPI patterns (in arbitrary units) for the $\mathcal{H}_1$ model with parameters $a = b = 1, t = -1.5, d = m = 0, \beta = 0.9$. We take $E = 0$, and $U = 1$.

where $d\boldsymbol{q} \equiv dq_x dq_z$ and

$$g(E, \boldsymbol{q}, \boldsymbol{k}) = G_s(E, \boldsymbol{q})T(E)G_s(E, \boldsymbol{q} - \boldsymbol{k})$$
$$- G_s^*(E, \boldsymbol{q} - \boldsymbol{k})T^*(E)G_s^*(E, \boldsymbol{q}). \quad (6)$$

We leave the derivation of Eqs. (5) and (6) to Appendix A.

In Fig. 2 we plot the resulting $\delta\rho(\boldsymbol{k}, E)$ as a function of momenta $\boldsymbol{k} = (k_x, k_z)$ at $E = 0$. First, note the central feature corresponding to intra-arc scattering processes, and second, the complete absence of any noncentral feature that could potentially arise from the interarc scattering processes. Given the spin structure of the two oppositely polarized Fermi arcs, such interarc scattering processes should indeed be forbidden, since that would require spin flips which cannot occur in the presence of a scalar scattering potential. For instance, in superconductors, scattering between states with opposite spins does not yield any QPI features [32]. It is surprising that SSP calculations in Ref. [6] indicate, however, a diminished but nonzero intensity in the interarc scattering features: As we show here, the full T-matrix approach seems to indicate that the interarc scattering is, in fact, zero. This difference probably stems from SSP yielding inaccurate results versus the T-matrix formalism [33], since the latter takes into account all-order scattering processes, unlike the former. The only nonzero observable intensity would appear in our approach in the presence of a magnetic impurity in the spin-polarized local density of states (LDOS), the same as in Ref. [32]. However, the present experiments do not measure the spin-polarized LDOS, and they observe nevertheless interarc scattering features. This makes us believe that the Hamiltonian for MoTe$_2$ presented in Ref. [6] does not model well the underlying spin structure. Furthermore, the elliptical shape of the central feature in Fig. 2 is very different from the eight-shaped one derived using SSP and JDOS.
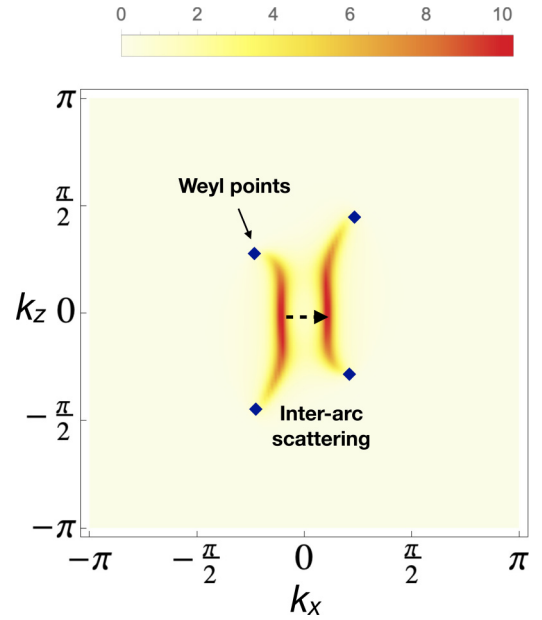

FIG. 3. The surface spectral function at $E = 0$ for the $\mathcal{H}_2$ model with parameters $a = b = 1$, $t = -1.5$, $\lambda = 0.5$, $d = 0.1$, $\alpha = 0.3$, and $\beta = 0.7$. We note the emergence of the two Fermi arcs.

We perform a similar analysis on a different Weyl semimetal model, introduced in Ref. [8]:

$$\mathcal{H}_2(\boldsymbol{k}) = g_1(\boldsymbol{k})\tau_1\sigma_3 + g_2(\boldsymbol{k})\tau_2\sigma_0 + g_3(\boldsymbol{k})\tau_3\sigma_0 + d\tau_2\sigma_3$$
$$+ \beta\tau_2\sigma_2 + \alpha\sin k_y\tau_1\sigma_2 + \lambda\sin k_z\tau_0\sigma_1. \quad (7)$$

We consider the values of the parameters similar to those in Ref. [8], thus we take $a = b = 1, t = -1.5, \lambda = 0.5, d = 0.1, \alpha = 0.3$, and $\beta = 0.7$. This configuration is also characterized by four Weyl points, and two Fermi arcs per surface. The resulting surface spectral function is depicted in Fig. 3.

For this model we also calculate the QPI patterns, shown in Fig. 4. Unlike in the Kourtis model [6], here the Fermi arcs have *nearly* opposite spins (the two opposing Fermi arcs may exhibit small regions with the same spin, as can be seen, for example, in Fig. 5 of Ref. [28]), and therefore, weak interarc scattering processes marked by a dotted rectangle are visible in Fig. 4. We note, however, that the intra-arc scattering still dominates in the QPI pattern.

III. SURFACE GREEN'S FUNCTIONS AND QPI PATTERNS IN THE MODEL OF MCCORMICK *et al.*

In what follows we consider the minimal helium model proposed in Ref. [7] to describe systems with four Weyl nodes, corresponding Fermi-arc surface states, impurity scattering, and the resulting QPI patterns. The Hamiltonian for such a model is given by

$$\mathcal{H}_3(\boldsymbol{k}) = \gamma[\cos(2k_x) - \cos(k_0)][\cos(k_z) - \cos(k_0)]\sigma_0$$
$$- m\{[1 - \cos^2(k_z) - \cos(k_y)]$$
$$+ 2t_x[\cos(k_x) - \cos(k_0)]\}\sigma_1$$
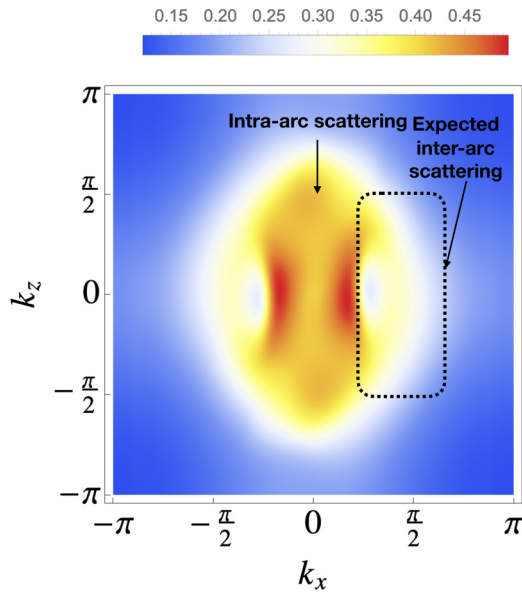$$- 2t\sin(k_y)\sigma_2 - 2t\cos(k_z)\sigma_3. \quad (8)$$

FIG. 4. QPI patterns in arbitrary units for the model $\mathcal{H}_2$ with $a = b = 1$, $t = -1.5$, $\lambda = 0.5$, $d = 0.1$, $\alpha = 0.3$, and $\beta = 0.7$. We take $E = 0$, and $U = 1$.

As opposed to the previous section, this model is defined in a single-orbital basis, $\psi(\mathbf{k}) = (c_{\mathbf{k}\uparrow}, c_{\mathbf{k}\downarrow})$. At $\gamma = 0$ it yields a Weyl semimetal with four nodes located at $(\pm k_0, 0, \pm \pi/2)$. A nonzero γ produces a tilting of the Weyl cones; when γ is sufficiently large (here, $\gamma_c = 2$), the modification of the Weyl cones is strong enough to generate four electron and four hole pockets that exist at $E = 0$ and meet at the Weyl nodes. There is also a trivial hole pocket centered at $k = (0, 0, 0)$ and a trivial electron pocket centered at $k = (\pi, 0, 0)$. In this type of systems some of the resulting surface states are topological, i.e., Fermi arcs, while the others, denoted "track states," are trivial. The latter form closed loops in momentum space. We consider two sets of parameters, the first, (a) $t = 1$, $k_0 = \pi/2$, $t_x = 1/2$, $m = 2$, $\gamma = 1.4$, exhibiting solely Fermi arcs, and the second, (b) $t = 1$, $k_0 = \pi/2$, $t_x = 1/2$, $m = 2$, $\gamma = 2.4$, with both Fermi arcs and track states. For each set we apply the technique introduced in Ref. [28] to recover the surface states (i.e., Fermi arcs and track states), and subsequently we use the surface GF obtained by this technique to study the QPI patterns. In Fig. 5 we plot the spectral function for the surface states $A(E, k_x, k_z) = -\frac{1}{\pi} \text{Im}\{\text{tr}[G_s(E, k_x, k_z)]\}$ for these two sets of parameters.

Focusing on one boundary (corresponding to that denoted in blue in Ref. [28]), we note in Fig. 5(a) the formation of two Fermi arcs roughly parallel to k_x, and in Fig. 5(b) that of two Fermi arcs in the k_y direction as well as of two sets of track states. Our results are fully consistent with those of Ref. [28], showing once more the versatility and simplicity of our method. Note again that our technique is fully analytical, the only "numerical" calculation to be performed is an integral of the Green's function over the Brillouin zone.

Once we have recovered the surface Green's functions, we proceed to the calculation of the QPI features in the presence of a single localized impurity. Exactly as in the previous
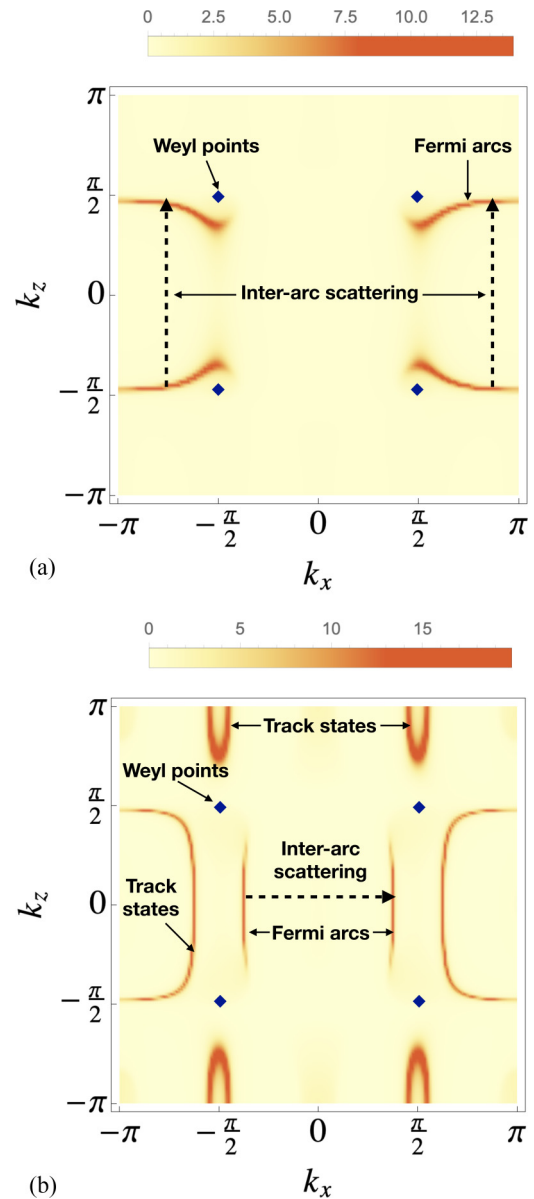

(a)

(b)

FIG. 5. The surface spectral function at $E = 0.25$ for the $\mathcal{H}_3$ model with parameters (a) $t = 1$, $k_0 = \pi/2$, $t_x = 1/2$, $m = 2$, $\gamma = 1.4$, and (b) $t = 1$, $k_0 = \pi/2$, $t_x = 1/2$, $m = 2$, $\gamma = 2.4$.

section we use the T-matrix approximation to obtain the Fourier transform of the LDOS, i.e., a quantity that can be compared to what is currently measured experimentally. In Fig. 6 we plot the resulting $\delta\rho(\mathbf{k}, E)$ as a function of $\mathbf{k}$ for $E = 0.25$ and the set of parameters of Fig. 5(a). We note the presence of a central feature which corresponds to the intra-Fermi-arc scattering, as well as a winglike feature centered around values of k_z slightly larger in absolute value than $\pi/2$, corresponding to interarc scattering. Note that, as opposed to the previous section, the interarc and intra-arc scattering features are of the same order of intensity.

In Fig. 7(a) we plot the QPI features observed for the other set of parameters, i.e., $t = 1$, $k_0 = \pi/2$, $t_x = 1/2$, $m = 2$, $\gamma = 2.4$, corresponding to the formation of both topological Fermi arcs and trivial track states. We note that the resulting
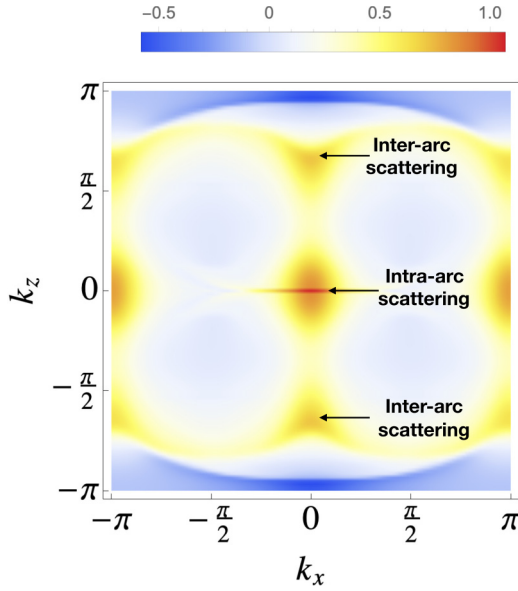
FIG. 6. QPI patterns in arbitrary units for the model $\mathcal{H}_3$ with $t = 1$, $k_0 = \pi/2$, $t_x = 1/2$, $m = 2$, $\gamma = 1.4$. We take $E = 0.25$, and $U = 1$.

QPI features are indeed very complex, since they correspond to both intra- and inter-Fermi-arc scattering, as well scattering inside and between different closed contours representing the track states, and also to the scattering between Fermi arc states and track states. To disentangle these features in Figs. 7(b) and 7(c) we plot "partial scattering integrals," i.e., performing the integral in Eq. (5) only over some parts of the Brillouin zone. Thus, in Fig. 7(b) we integrate over q only over the region $-\pi/2 < q_x < -\pi/4$, $-\pi/2 < q_z < \pi/2$, such that we only take into account the scattering of the states belonging to one Fermi arc with the rest of the Brillouin zone (BZ). We therefore eliminate the contributions to the total weight coming from scattering between the track states, and we are left with intra-Fermi-arc scattering, inter-Fermi-arc scattering, as well as scattering between Fermi-arc states and track states; these, however, can be easily identified based on their wave vectors. We mark each of these processes by black arrows in the figure. Similarly, in Fig. 7(c) we integrate over q only over the region $-\pi < q_x < -\pi/2$, $-\pi/2 < q_z < \pi/2$, such that we only take into account the scattering of the states over one track state with the rest of the BZ. Each type of scattering process is identified in the figure with the resulting features.

Note that the intra-arc scattering is greatly suppressed for this regime compared to the interarc scattering.

IV. CONCLUSION

We have used an analytical technique introduced in Ref. [28] and the T-matrix formalism to calculate the surface Green's functions as well as the QPI patterns for several different models describing Weyl semimetals. For the Kourtis and Lau models [6,8] we found that no interarc interference patterns and correspondingly very weak interference patterns arise, in contrast to original predictions based on JDOS and SSP calculations. For the minimal McCormick model [7] both interarc and intra-arc scattering features are visible for type
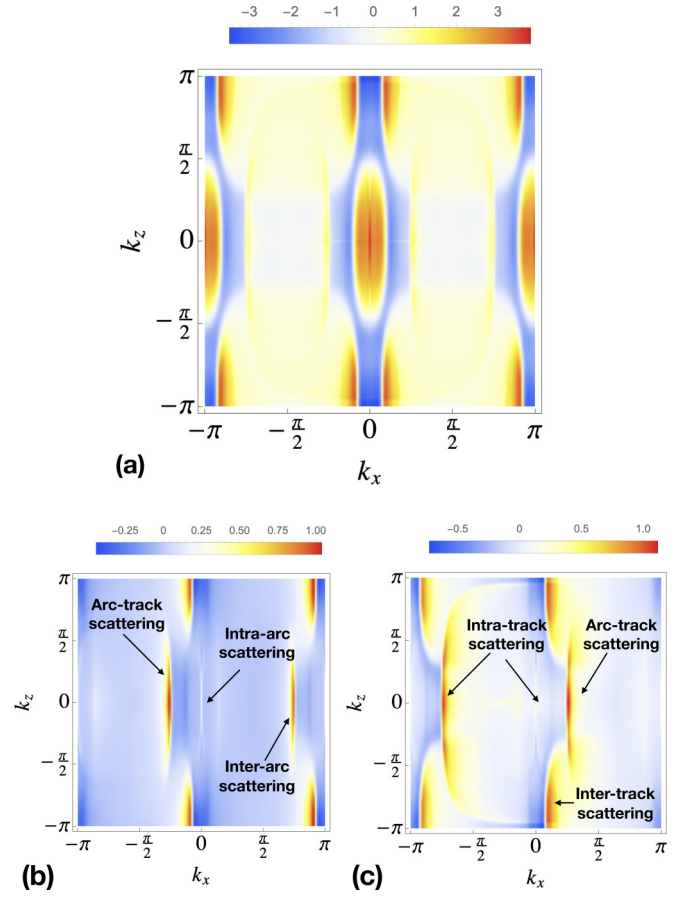

FIG. 7. QPI patterns in arbitrary units for the model $\mathcal{H}_3$ with $t = 1$, $k_0 = \pi/2$, $t_x = 1/2$, $m = 2$, $\gamma = 2.4$. We take $E = 0.25$, and $U = 1$. (a) Full QPI pattern, i.e. scattering integrated over the full BZ, (b) q integrated only over the region $-\pi/2 < q_x < -\pi/4$, $-\pi/2 < q_z < \pi/2$, (c) q integrated only over the region $-\pi < q_x < -\pi/2$, $-\pi/2 < q_z < \pi/2$.

I models, as well as scattering between the track states and the Fermi-arc states and intratrack scattering for the type II models.

We stress once more that the technique proposed in Ref. [28] is very well suited to describe analytically the surface Green's functions for complex tight-binding bulk models, and it requires no iterative numerical calculations. As demonstrated here, the resulting Green's functions can very easily and straightforwardly be used to calculate the surface QPI features.

APPENDIX A: QPI PATTERN DERIVATION

In this Appendix, we first derive Eqs. (5) and (6), and second, we show how to extend this formalism to the case of double-impurity scattering.
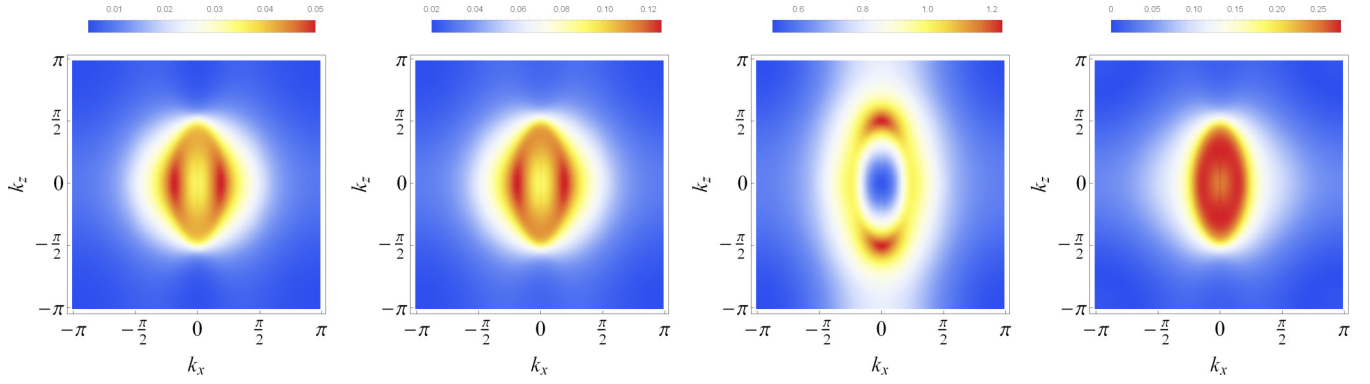
FIG. 8. QPI patterns in arbitrary units for the Kourtis model calculated for scalar impurities with varying strength U. From left to right, we set $U = 0.5$, $U = 1$, $U = 3$, and $U = 10$.

1. Single-impurity scattering

To compute quasiparticle interference patterns in a system of dimension d we take an unperturbed system described by a retarded Green's function $G_0(E, \boldsymbol{r})$ and we introduce a localized impurity potential, $V\delta(\boldsymbol{r})$, $\boldsymbol{r} \in \mathbb{R}^d$. The perturbed Green's function in the presence of such an impurity can be expressed via the T matrix,

$$G(E, \boldsymbol{r}, \boldsymbol{r}') = G_0(E, \boldsymbol{r} - \boldsymbol{r}') + G_0(E, \boldsymbol{r})T(E)(E, -\boldsymbol{r}'),$$
(A1)

where the T matrix

$$T(E) = [\mathbb{I} - VG_0(E, \boldsymbol{r} = 0)]^{-1}V$$

$$\equiv \left[\mathbb{I} - V\int \frac{d\boldsymbol{k}}{(2\pi)^d}G_0(E, \boldsymbol{k})\right]^{-1}V$$
(A2)

takes into account the cumulative effect of all-order impurity scattering processes. The correction to the local density of states in the presence of impurity can be written in terms of the perturbed Green's function as follows,

$$\delta\rho(E, \boldsymbol{r}) \equiv -\frac{1}{\pi}\mathrm{Im}\,\mathrm{tr}[G(E, \boldsymbol{r}, \boldsymbol{r}) - G_0(E, \boldsymbol{0})]$$

$$= -\frac{1}{\pi}\mathrm{Im}\,\mathrm{tr}[G_0(E, \boldsymbol{r})T(E)G_0(E, -\boldsymbol{r})].$$
(A3)

Finally, to obtain QPI patterns in the momentum space we need to Fourier transform the equation above, i.e., to calculate $\delta\rho(E, \boldsymbol{k}) = \int d\boldsymbol{r}\, \delta\rho(E, \boldsymbol{r})e^{-i\boldsymbol{k}\cdot\boldsymbol{r}}$. We rewrite the imaginary part using the identity $\mathrm{Im}\,z = \frac{1}{2i}(z - z^*)$ and we get

$$\delta\rho(E, \boldsymbol{k}) = -\frac{1}{2\pi i}\mathrm{tr}\int d\boldsymbol{r}[G_0(E, \boldsymbol{r})T(E)G_0(E, -\boldsymbol{r})$$

$$- G_0^*(E, \boldsymbol{r})T^*(E)G_0^*(E, -\boldsymbol{r})]e^{-i\boldsymbol{k}\cdot\boldsymbol{r}} = \star.$$

Next, we express the unperturbed Green's functions in the integrand via the Fourier transform,

$$\star = -\frac{1}{2\pi i}\mathrm{tr}\int \frac{\boldsymbol{q}}{(2\pi)^d}\int \frac{\tilde{\boldsymbol{q}}}{(2\pi)^d}[G_0(E, \boldsymbol{q})T(E)G_0(E, \tilde{\boldsymbol{q}}) - G_0^*(E, \tilde{\boldsymbol{q}})T^*(E)G_0^*(E, \boldsymbol{q})]\int \boldsymbol{r}\, e^{i\boldsymbol{q}\cdot\boldsymbol{r}}e^{-i\tilde{\boldsymbol{q}}\cdot\boldsymbol{r}}e^{-i\boldsymbol{k}\cdot\boldsymbol{r}}$$

$$= -\frac{1}{2\pi i}\mathrm{tr}\int \frac{\boldsymbol{q}}{(2\pi)^d}\int \frac{\tilde{\boldsymbol{q}}}{(2\pi)^d}[G_0(E, \boldsymbol{q})T(E)G_0(E, \tilde{\boldsymbol{q}}) - G_0^*(E, \tilde{\boldsymbol{q}})T^*(E)G_0^*(E, \boldsymbol{q})] \times (2\pi)^d\delta(\boldsymbol{q} - \tilde{\boldsymbol{q}} - \boldsymbol{k})$$

$$= -\frac{1}{2\pi i}\mathrm{tr}\int \frac{\boldsymbol{q}}{(2\pi)^d}[G_0(E, \boldsymbol{q})T(E)G_0(E, \boldsymbol{q} - \boldsymbol{k}) - G_0^*(E, \boldsymbol{q} - \boldsymbol{k})T^*(E)G_0^*(E, \boldsymbol{q})] = \frac{i}{2\pi}\int \frac{d\boldsymbol{q}}{(2\pi)^d}g(E, \boldsymbol{q}, \boldsymbol{k}),$$

where we defined

$$g(E, \boldsymbol{q}, \boldsymbol{k}) \equiv \mathrm{tr}[G_0(E, \boldsymbol{q})T(E)G_0(E, \boldsymbol{q} - \boldsymbol{k})$$

$$- G_0^*(E, \boldsymbol{q} - \boldsymbol{k})T^*(E)G_0^*(E, \boldsymbol{q})],$$
(A4)

which corresponds to Eq. (6). Since in the main text we are dealing with QPI patterns on a surface, we set $d = 2$ and we get Eq. (5):

$$\delta\rho(E, \boldsymbol{k}) = \frac{i}{2\pi}\int \frac{d\boldsymbol{q}}{(2\pi)^2}g(E, \boldsymbol{q}, \boldsymbol{k}).$$
(A5)

The unperturbed retarded Green's function $G_0(E, \boldsymbol{q})$ is given by the analytical continuation of the Matsubara Green's function $\mathcal{G}(i\omega_n, \boldsymbol{q}) = [i\omega_n - \mathcal{H}(\boldsymbol{q})]^{-1}$, with $i\omega_n \to E + i\delta$. In all of our simulations we have considered $\delta = 0.05$.

2. Double-impurity scattering

Below we examine the case of a double impurity. The T-matrix formalism can be modified to include scattering from both impurities [33,34]. Assuming that the impurities are localized at $\boldsymbol{r}_0$ and $\boldsymbol{r}_1$, we write the correction to the perturbed Green's function as follows,

$$\delta G(E, \boldsymbol{r}_i, \boldsymbol{r}_j) = \sum_{\alpha, \beta = 0, 1} G_0(E, \boldsymbol{r}_i, \boldsymbol{r}_\alpha)T_{\alpha\beta}(E)G_0(E, \boldsymbol{r}_\beta, \boldsymbol{r}_j),$$
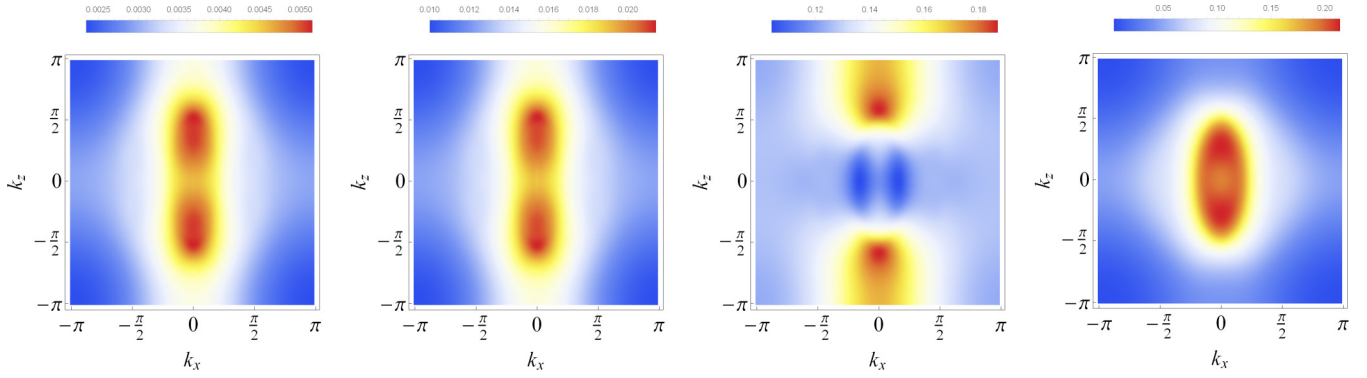(A6)

FIG. 9. QPI patterns in arbitrary units for the Kourtis model calculated for magnetic impurities with varying strength U. From left to right, we set $U = 0.5$, $U = 1$, $U = 3$, and $U = 10$.

where α and β run over the two impurities, and $T_{\alpha\beta}(E)$ is the real-space T-matrix,

$$T_{\alpha\beta}(E, \boldsymbol{r}_\alpha, \boldsymbol{r}_\beta) = [\mathbb{I} - V G_0(E, \boldsymbol{r}_\alpha - \boldsymbol{r}_\beta)]^{-1}V$$

$$= \left[\mathbb{I} - V \int \frac{d\boldsymbol{k}}{(2\pi)^2} G_0(E, \boldsymbol{k})e^{i\boldsymbol{k}\cdot(\boldsymbol{r}_\alpha - \boldsymbol{r}_\beta)}\right]^{-1}V.$$

$$(A7)$$

By rewriting Eq. (A6) in momentum space, one can obtain a T-matrix formula representing scattering by both impurities,

$$T(E, \boldsymbol{k}, \boldsymbol{k}') = \sum_{\alpha,\beta=0,1} e^{i(\boldsymbol{k}'\cdot\boldsymbol{r}_\beta - \boldsymbol{k}\cdot\boldsymbol{r}_\alpha)}T_{\alpha\beta}(E, \boldsymbol{r}_\alpha, \boldsymbol{r}_\beta), \quad (A8)$$

and the formula for g in Eq. (5) is modified to

$$g(E, \boldsymbol{q}, \boldsymbol{k}) = G_0(E, \boldsymbol{q})T(E, \boldsymbol{q}, \boldsymbol{q} - \boldsymbol{k})G_0(E, \boldsymbol{q} - \boldsymbol{k})$$
$$- G_0^*(E, \boldsymbol{q} - \boldsymbol{k})T^*(E, \boldsymbol{q} - \boldsymbol{k}, \boldsymbol{q})G_0^*(E, \boldsymbol{q}). \quad (A9)$$
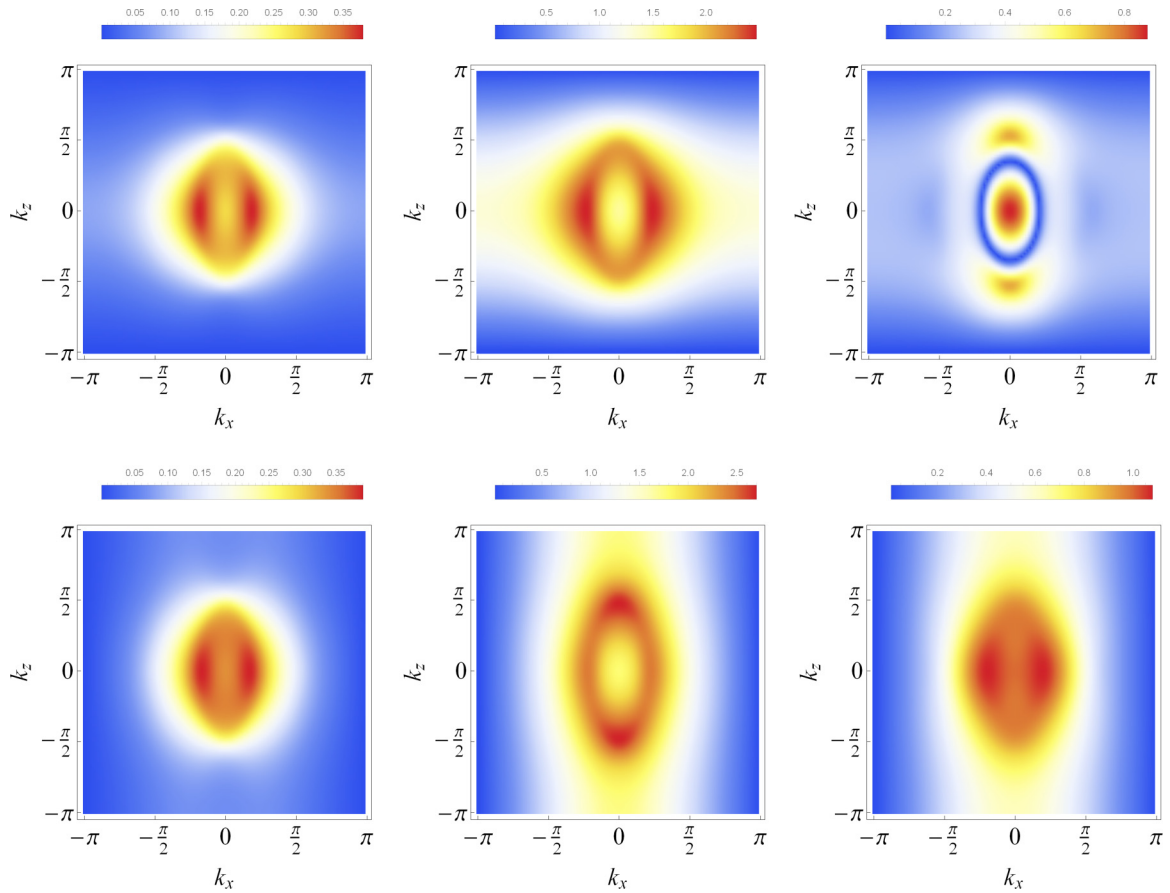

FIG. 10. QPI patterns in arbitrary units for the Kourtis model calculated for two impurities with different strength U. In the left column we set $U = 1$, while in the central and right columns we chose $U = 3$ and $U = 10$, respectively. For the first row we set $\boldsymbol{r}_0 = (x = 0, z = 0)$ and $\boldsymbol{r}_1 = (x = 0, z = 1)$, and for the second one, $\boldsymbol{r}_1 = (x = 1, z = 0)$.

APPENDIX B: STUDY OF DIFFERENT SCATTERING IMPURITIES FOR THE KOURTIS MODEL

In this Appendix we show the effects of various scattering impurities on the QPI pattern for the Kourtis model in Eq. (2).

1. Single scalar or magnetic impurity

We first study the QPI patterns for a single scalar impurity $V = U\mathbb{I}$ with different values for the impurity strength U. The results are shown in Fig. 8. We find that changing U modifies the shape of the intra-arc scattering features. However, no interarc scattering appears.

We now consider a magnetic impurity, $V = U \operatorname{diag}\{1, -1, 1, -1\}$, where "diag" stands for a diagonal

matrix. The choice of basis corresponds to the one in Eq. (1), i.e., $(c_{kA\uparrow}, c_{kA\downarrow}, c_{kB\uparrow}, c_{kB\downarrow})$. The QPIs obtained are shown in Fig. 9. For a strong enough impurity, i.e., $U = 10$, the intra-arc pattern resembles the one obtained with a scalar impurity. For lower values of U, the pattern's shape is quite different, but we still do not find any interarc scattering.

2. Double impurity

QPI patterns for a double impurity localized at $\boldsymbol{r}_0 = (x = 0, z = 0)$, and $\boldsymbol{r}_1 = (x = 0, z = 1)$ or $\boldsymbol{r}_1 = (x = 1, z = 0)$ are demonstrated in Fig. 10. We find slightly different shapes for the intra-arc scattering features, nevertheless we observe no interarc scattering.

[1] A. M. Turner and A. Vishwanath, in *Contemporary Concepts of Condensed Matter Science* (Elsevier, Amsterdam, 2013), pp. 293–324.

[2] A. K. Mitchell and L. Fritz, Phys. Rev. B **93**, 035137 (2016).

[3] A. Gyenis, H. Inoue, S. Jeon, B. B. Zhou, B. E. Feldman, Z. Wang, J. Li, S. Jiang, Q. D. Gibson, S. K. Kushwaha, J. W. Krizan, N. Ni, R. J. Cava, B. A. Bernevig, and A. Yazdani, New J. Phys. **18**, 105003 (2016).

[4] F. Lambert, A. P. Schnyder, R. Moessner, and I. Eremin, Phys. Rev. B **94**, 165146 (2016).

[5] G. Chang, S.-Y. Xu, H. Zheng, C.-C. Lee, S.-M. Huang, I. Belopolski, D. S. Sanchez, G. Bian, N. Alidoust, T.-R. Chang, C.-H. Hsu, H.-T. Jeng, A. Bansil, H. Lin, and M. Z. Hasan, Phys. Rev. Lett. **116**, 066601 (2016).

[6] S. Kourtis, J. Li, Z. Wang, A. Yazdani, and B. A. Bernevig, Phys. Rev. B **93**, 041109(R) (2016).

[7] T. M. McCormick, I. Kimchi, and N. Trivedi, Phys. Rev. B **95**, 075133 (2017).

[8] A. Lau, K. Koepernik, J. van den Brink, and C. Ortix, Phys. Rev. Lett. **119**, 076801 (2017).

[9] Q. Xu, E. Liu, W. Shi, L. Muechler, J. Gayles, C. Felser, and Y. Sun, Phys. Rev. B **97**, 235416 (2018).

[10] H. Zheng and M. Z. Hasan, Adv. Phys.: X **3**, 1466661 (2018).

[11] S. Jeon, B. B. Zhou, A. Gyenis, B. E. Feldman, I. Kimchi, A. C. Potter, Q. D. Gibson, R. J. Cava, A. Vishwanath, and A. Yazdani, Nat. Mater. **13**, 851 (2014).

[12] K. Deng, G. Wan, P. Deng, K. Zhang, S. Ding, E. Wang, M. Yan, H. Huang, H. Zhang, Z. Xu, J. Denlinger, A. Fedorov, H. Yang, W. Duan, H. Yao, Y. Wu, S. Fan, H. Zhang, X. Chen, and S. Zhou, Nat. Phys. **12**, 1105 (2016).

[13] H. Zheng, S.-Y. Xu, G. Bian, C. Guo, G. Chang, D. S. Sanchez, I. Belopolski, C.-C. Lee, S.-M. Huang, X. Zhang, R. Sankar, N. Alidoust, T.-R. Chang, F. Wu, T. Neupert, F. Chou, H.-T. Jeng, N. Yao, A. Bansil, S. Jia, H. Lin, and M. Z. Hasan, ACS Nano **10**, 1378 (2016).

[14] H. Zheng, G. Bian, G. Chang, H. Lu, S.-Y. Xu, G. Wang, T.-R. Chang, S. Zhang, I. Belopolski, N. Alidoust, D. S. Sanchez, F. Song, H.-T. Jeng, N. Yao, A. Bansil, S. Jia, H. Lin, and M. Z. Hasan, Phys. Rev. Lett. **117**, 266804 (2016).

[15] H. Inoue, A. Gyenis, Z. Wang, J. Li, S. W. Oh, S. Jiang, N. Ni, B. A. Bernevig, and A. Yazdani, Science **351**, 1184 (2016).

[16] R. Batabyal, N. Morali, N. Avraham, Y. Sun, M. Schmidt, C. Felser, A. Stern, B. Yan, and H. Beidenkopf, Sci. Adv. **2**, e1600709 (2016).

[17] W. Zhang, Q. Wu, L. Zhang, S.-W. Cheong, A. A. Soluyanov, and W. Wu, Phys. Rev. B **96**, 165125 (2017).

[18] P. Deng, Z. Xu, K. Deng, K. Zhang, Y. Wu, H. Zhang, S. Zhou, and X. Chen, Phys. Rev. B **95**, 245110 (2017).

[19] C.-L. Lin, R. Arafune, R.-Y. Liu, M. Yoshimura, B. Feng, K. Kawahara, Z. Ni, E. Minamitani, S. Watanabe, Y. Shi, M. Kawai, T.-C. Chiang, I. Matsuda, and N. Takagi, ACS Nano **11**, 11459 (2017).

[20] Y. Yuan, X. Yang, L. Peng, Z.-J. Wang, J. Li, C.-J. Yi, J.-J. Xian, Y.-G. Shi, and Y.-S. Fu, Phys. Rev. B **97**, 165435 (2018).

[21] C.-L. Lin, R. Arafune, E. Minamitani, M. Kawai, and N. Takagi, J. Phys.: Condens. Matter **30**, 105703 (2018).

[22] N. Morali, R. Batabyal, P. K. Nag, E. Liu, Q. Xu, Y. Sun, B. Yan, C. Felser, N. Avraham, and H. Beidenkopf, Science **365**, 1286 (2019).

[23] P. Sessi, F.-R. Fan, F. Küster, K. Manna, N. B. M. Schröter, J.-R. Ji, S. Stolz, J. A. Krieger, D. Pei, T. K. Kim, P. Dudin, C. Cacho, R. Widmer, H. Borrmann, W. Shi, K. Chang, Y. Sun, C. Felser, and S. S. P. Parkin, Nat. Commun. **11**, 3507 (2020).

[24] W. Ziegler, D. Poilblanc, R. Preuss, W. Hanke, and D. J. Scalapino, Phys. Rev. B **53**, 8704 (1996).

[25] M. I. Salkola, A. V. Balatsky, and D. J. Scalapino, Phys. Rev. Lett. **77**, 1841 (1996).

[26] G. D. Mahan, *Many-Particle Physics* (Springer, New York, 2000).

[27] C. Bena, C. R. Phys. **17**, 302 (2016).

[28] S. Pinon, V. Kaladzhyan, and C. Bena, Phys. Rev. B **101**, 115405 (2020).

[29] Note that the impurity needs to contain a number of planes equal to the unit cell number of planes in the model, or more in case of higher-order hopping between planes.

[30] A. V. Balatsky, I. Vekhter, and J.-X. Zhu, Rev. Mod. Phys. **78**, 373 (2006).

[31] C. Bena, Phys. Rev. Lett. **100**, 076601 (2008).

[32] V. Kaladzhyan, P. Simon, and C. Bena, Phys. Rev. B **94**, 134511 (2016).

[33] P. G. Derry, A. K. Mitchell, and D. E. Logan, Phys. Rev. B **92**, 035126 (2015).

[34] A. K. Mitchell, P. G. Derry, and D. E. Logan, Phys. Rev. B **91**, 235127 (2015).